ASME Journal of Turbomachinery
Online journal at:
https://asmedigitalcollection.asme.org/turbomachinery

Sofía I. Medina Cassillas[1]
Whittle Laboratory,
University of Cambridge,
1 JJ Thomson Avenue,
Cambridge CB3 0DY, UK
e-mail: sim31@cam.ac.uk

Alejandro Castillo Pardo[2]
Whittle Laboratory,
University of Cambridge,
1 JJ Thomson Avenue,
Cambridge CB3 0DY, UK
e-mail: a.castillo.pardo@outlook.com

Cesare A. Hall
Whittle Laboratory,
University of Cambridge,
1 JJ Thomson Avenue,
Cambridge CB3 0DY, UK
e-mail: cah1003@cam.ac.uk

Ben Mohankumar[3]
Rolls-Royce plc,
Derbyshire DE24 7XX, UK
e-mail: Benjamin.Mohankumar@Rolls-Royce.com

Effect of Blade Damage on Low Pressure Ratio Fan Windmill Aerodynamics

Fan windmill occurs when power to a turbofan is cut during flight and the airflow through the engine causes the fan to freewheel, often following fan damage. The fan rotational speed and drag during windmill determine the loads transmitted to the airframe, and these depend on the fan damage sustained. Idealized patterns of axisymmetric and non-axisymmetric damage have been studied using high-resolution measurements in a flow-field representative of a low pressure ratio fan in combination with steady Reynolds-averaged Navier–Stokes (RANS) simulations to understand the impact on the windmill flow field. Axisymmetric tip damage decreases the windmill rotational speed by 61% when 25% of the blade span is removed due to a shift in the zero-work radius. The reduced blade span creates an intense tip vortex and redistributes the flow, increasing the axial velocity above the damaged tip. For non-axisymmetric damage, there is still work output at the blade tip, such that removing 25% of half the blades with varying damage pitch to chord reduces the fan rotational speed by 9–13% compared to undamaged windmill. Phase-averaged hot-wire measurements show that this additional rotor work is due to radial flow redistribution combined with turning of the flow in the passages above the damaged blades.
[DOI: 10.1115/1.4067518]

Keywords: compressor stall, surge and operability, computational fluid dynamics (CFD), fan aerodynamic design, measurement techniques, turbomachinery blading design

Introduction

The windmill condition occurs after the in-flight shutdown of a turbofan when the ram pressure of the oncoming air causes the fan to freewheel. Fan windmill often follows damage to the fan due to foreign object ingestion, birdstrike, or a fan blade off failure. Figure 1 shows the key windmill flow features for an undamaged fan and for a fan with axisymmetric tip damage based on single-passage computational fluid dynamics (CFD) results. Pressure side separation extends across most of the span and produces a vortex that migrates toward the casing. In the undamaged case, this combines with the casing flow to form a large streamwise vortex, which is the main source of loss. Over much of the span, flow reattachment occurs toward the trailing edge leading to low deviation, as also shown in Refs. [1–3]. In the axisymmetric damage case, a smaller, streamwise vortex forms at the lower radius blade tip and there is increased axial flow velocity above this.

Prior knowledge of the windmill drag and rotational speed is crucial for airframe designers because the drag force of the engine at windmill influences the size of the aircraft vertical stabilizer and the fan rotational speed determines the loads transmitted to the aircraft. The windmill condition will become even more critical for future engine designs with a lower fan pressure ratio, which drives up the fan diameter, increasing drag and lowering windmill rotational speed. Currently, engine manufacturers predict the windmill operating point using a throughflow method. This has been validated for undamaged fans but does not consider the 3D effects shown in Fig. 1 or flow non-axisymmetry which will be significant if the fan is damaged.

Previous research into fan windmill has focused on characterizing the flow field for an undamaged fan. It has been widely shown that for a fan at windmill, the inner sections of the span operate as a compressor and the outer sections as a turbine such that no work is produced [1,2,4]. The fan rotational speed at windmill is dependent only on the mass flow through the fan, such that there is a constant windmill flow coefficient and flow similarity at every mass flowrate [5–7]. This mass flowrate is dependent on the losses through the fan stage, which are dominated by flow separation on both the rotor and stator pressure sides due to the low rotational speed of the fan, which leads to high negative incidence [1–3].

Few studies have focused on the effects of fan damage on the windmill flow field. When the damage to the blade tips is non-axisymmetric, it might be expected that the rotor flow field would simply be a combination of those shown in Fig. 1. However, Mohankumar and Wilson [8] numerically investigated the effect of axisymmetric and nonaxisymmetric damage on the fan rotational speed and found that this is not the case. Axisymmetric damage causes a large reduction in windmill blade speed due to the

[1]Corresponding author.
[2]Present address: Airbus, Toulouse, France.
[3]Present address: Mathworks, Cambridge, UK.

Contributed by International Gas Turbine Institute (IGTI) of ASME for publication in the Journal of Turbomachinery. Manuscript received September 11, 2024; final manuscript received November 19, 2024; published online February 14, 2025. Tech. Editor: David G. Bogard.

removal of tip sections that would normally extract work from the flow. For non-axisymmetric damage cases, however, they found that the rotational speed increases with respect to an axisymmetric damage case with the equivalent amount of damage. This suggests that there are blade-to-blade interactions which are not understood. This was also indicated by Zhang et al. [9], who ran simulations of a windmilling fan with a missing blade and adjacent blade tip and found that the flow coefficient was nearly unchanged from an undamaged case.

These blade-to-blade effects observed in damaged fans introduce high uncertainties in the current throughflow method used in windmill prediction. This article will provide a detailed analysis of the windmill flow field for various non-axisymmetric fan damage patterns in order to determine the key parameters driving the windmill drag and rotational speed. It will be shown that although the flow blockage in non-axisymmetric cases could be approximated from axisymmetric damage, there are important blade-to-blade effects that modify the rotor work distribution. These findings provide a basis for improvements in the prediction of the windmill condition for realistic fan damage.

This article is the first detailed experimental and computational study of both axisymmetric and non-axisymmetric damage on fan windmill aerodynamics. The article starts by describing the fan windmill test rig and the damage test cases. The measurement techniques applied and the computational methods used to complement the experiment are then presented. These methods are first applied to understand the work and loss for an axisymmetric damage case. Test results from several non-axisymmetric damage cases are then compared to the axisymmetric damage and undamaged cases. Hot-wire measurements in the rotor relative frame are used to resolve the blade-to-blade effects and the changes in the rotor work distribution.

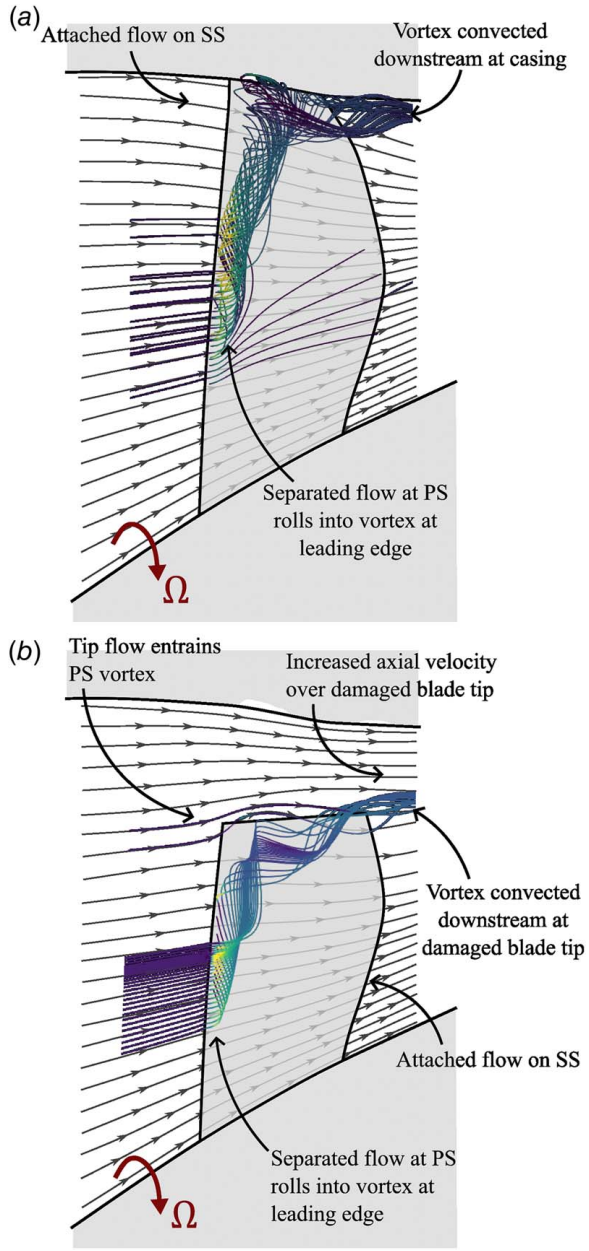

Fig. 1 Main flow features at windmill for undamaged (*a*) and axisymmetric tip damage (*b*) fan

A Low Pressure Ratio Fan Rig for Testing at Windmill Condition

The low-speed fan rig used for this study is shown in Fig. 2. The facility was developed in previous research for the study of boundary layer ingesting fans [10,11] and needed to be adapted to be representative of a low pressure ratio fan at windmill. The fan stage was redesigned and, to achieve the windmill condition, flow was drawn through the rig by an array of fans installed downstream of the working section.

The new fan design was developed using the streamline equilibrium throughflow method from Denton [12] to rapidly simulate the flow field at windmill, comparing the results to a high-speed rig and iterating the design until a good match was obtained. The following modifications were applied:

- Blade metal angles: The rotor and stator blade metal angles (χ_{LE} and χ_{TE}) were matched to the high-speed design to give the same rotor work distribution and a similar amount of pressure-side separation, and thus blockage, on the rotor and stator.
- Pitch-to-chord ratio: The blade pitch-to-chord ratio ($s/c = 2\pi r/(Nc)$) was set such that the blockage due to the

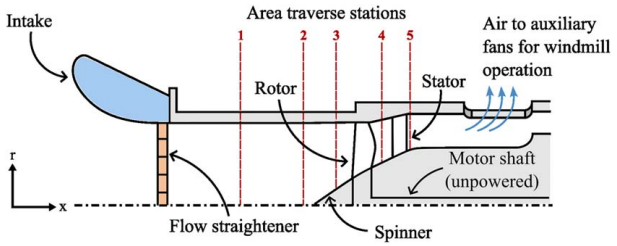

Fig. 2 Low-speed rig test facility

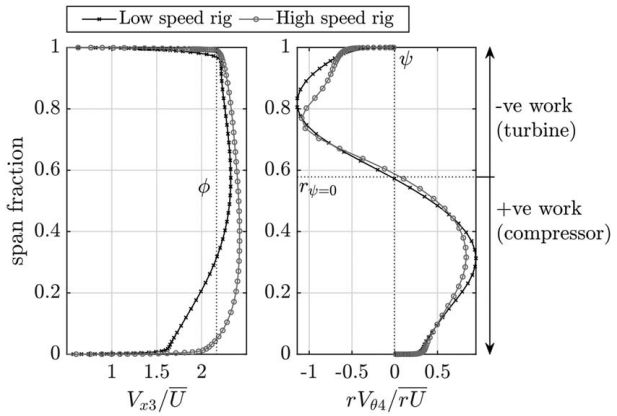

Fig. 3 Low-speed versus high-speed rig CFD at windmill

Table 1 Comparison of key parameters for low-speed rig and high-speed rig at windmill

		High-speed rig (CFD)	Low-speed rig (CFD)	Low-speed rig (EXP)
Tip Mach number	$M_{tip} = U_{tip}/\sqrt{\gamma RT}$	0.22	0.17	0.03
Tip Reynolds number	$Re_{tip} = \rho U_{tip} c_{tip}/\mu$	3.6×10^5	2.5×10^5	0.23×10^5
Flow coefficient	$\phi = \overline{V}_{x3}/\overline{U}$	2.15	2.21	2.19
Stage loading coefficient	$\psi = \overline{rV}_{\theta 4}/\overline{rU}$	0.013	0.003	−0.008

pressure side separation and the blade loading would be similar to those in the high-speed design.
- Hub line: The rig hub line was lowered in order to achieve a representative hub-to-tip ratio. The final low-speed design included a spinner upstream of the rotor, with $r_{hub}/r_{cas} = 0.309$.
- Casing line: The casing line was specified to match the contraction over the rotor blade and the diffusion upstream of the stator blade in the high-speed design.

The flow fields of the high-speed rig and the redesigned rig at windmill are detailed in Fig. 3. This shows a good match in terms of both the spanwise flow coefficient distribution $V_{x3}/\overline{U}$ and the spanwise work distribution $rV_{\theta 4}/\overline{rU}$. This ensures that the rotor zero-work point is matched between the designs, and there will be a similar incidence onto the rotor blades.

Table 1 summarizes the key parameters of the two designs at windmill for an undamaged fan rotor. This shows the high flow coefficient and the near-zero work input at windmill. Although the experiment is run at a lower Mach number than that of the CFD, it has been shown in the literature that at windmill there is mass flow similarity, such that the change in Mach number will not alter the flow field and, thus, it is valid to compare cases at different Mach numbers [2,7]. Both CFD and experiment are at such low speed that there will be no compressibility effects.

The redesign of the rig required the manufacture of new liners to achieve the modified annulus lines, and completely new rotor and stator blade rows. The rotor, shown in Fig. 4, was manufactured as a hub to which rotor blades can be attached. The rotor blades can therefore be fully replaced between tests in a short amount of time. This allowed for the rapid testing of many different patterns of fan damage, such as fanblade-off cases, damage to the blade tip, and various non-axisymmetric damage patterns.

(a)

(b)

Fig. 4 Low-speed rig fan. (*a*) Undamaged rotor. (*b*) Example damaged rotor, $A_D = 0.17$ and $n_D = 1$ (Fig. 5(c)).

Choice of Damage Patterns

To identify the key flow physics, idealized axisymmetric and non-axisymmetric damage patterns were designed such that it is possible to vary both the amount and distribution of damage around the annulus. Although these are idealized damage patterns, they will provide a detailed understanding of what influences the windmill operating point, which can be extended to more realistic damage cases, such as damaged sector or fan blade-off.

The rotor pressure side casing vortex was seen to have an effect on the work distribution, which is driving the rotational speed of the fan, as well as being the main source of loss in the rotor. Damaging the tip of the blades is therefore likely to lead to the largest changes in the windmill flow field as it will remove sections of the blade where the casing vortex would form. Both axisymmetric and non-axisymmetric tip damage patterns were used, where the non-axisymmetric damage cases were chosen to be a combination of the undamaged and axisymmetric tip damage cases. This allows comparing the results from non-axisymmetric cases to an average of the axisymmetric fans to assess how blade-to-blade interactions affect the windmill flow field.

Fan blade-off cases are not included in this study, as Zhang et al. [9] have shown previously that removing a single blade will not significantly change the operating point of the fan at windmill, and this has also been observed by the authors. However, the results from the damage cases studied can easily be extended to more nonaxisymmetric cases once the driving parameters for the windmill operating point are determined.

The full matrix of damage cases tested is shown in Fig. 5. A_D represents the fraction of the fan face area that has been removed through damage, Eq. (1) ($A_D = 0$ represents an undamaged fan and $A_D = 0.34$ is the axisymmetric damage case, where all the blade tips have been removed above 75% span). The number of consecutive damaged blades in a nonaxisymmetric damage case is n_D and the pitch-to-chord ratio above damaged blades $(s/c)_D$ is defined in Eq. (2)

$$A_D = \frac{N_D}{N} \times \frac{r_{cas}^2 - r_D^2}{r_{cas}^2 - r_{hub}^2} \tag{1}$$

$$\left(\frac{s}{c}\right)_D = \frac{2\pi r_{cas}}{N c_{cas}} \times (n_D + 1) \tag{2}$$

Table 2 summarizes the damage parameters and windmill flow coefficient for the fans tested. Note that the nonaxisymmetric damage cases have a flow coefficient (and therefore blade speed) which is much closer to the undamaged case than the axisymmetric damage case.

Measurement Techniques

Measurements were taken in the low-speed rig at the five locations shown in Fig. 2 using a five-hole pneumatic probe and a hot wire. Five-hole probe measurements were used to obtain the overall fan performance and pitchwise average profiles at the

Table 2 Damage pattern parameters and measured windmill flow coefficient

	A_D	n_D	$(s/c)_D$	ϕ
Undamaged (Fig. 5(*a*))	0	–	1.35	2.19
Axisymmetric tip damage (Fig. 5(*b*))	0.34	–	–	5.59
	0.17	1	2.70	2.64
Non-axisymmetric tip damage (Figs. 5(*c*)–5(*f*))	0.17	2	4.04	2.76
	0.17	3	5.39	2.77
	0.22	2	4.04	3.14

different traverse stations, whereas hot-wire measurements were used to resolve blade-to-blade variations in the rotor relative frame of reference.

The five-hole probe was calibrated in a dedicated wind tunnel for flow speed, yaw, and pitch. The hot wire was calibrated using King's law to relate hot-wire voltage E to flow velocity V as per Eq. (3), as recommended by Bruun [13]. The tangential flow angle was found at each point in the traverse by rotating the hot wire and then fitting a cosine curve through the points, as shown in Fig. 6. 20-dB gain, a 300-kHz low pass filter, and a 1-Hz high pass filter were used to improve the hot-wire signal-to-noise ratio

$$E^2 = E_0^2 + AV^b \tag{3}$$

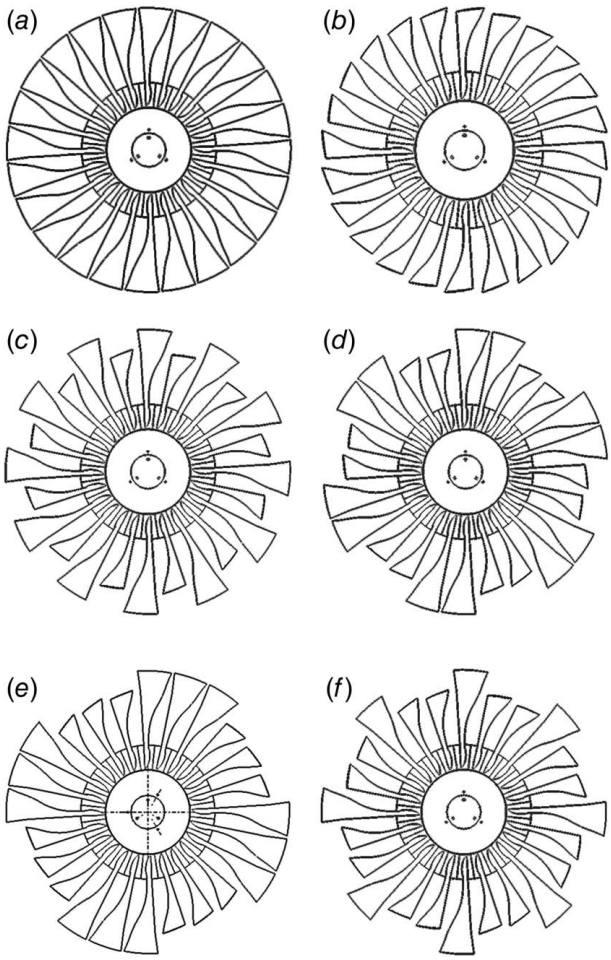

Fig. 5 Axisymmetric and non-axisymmetric damaged fan patterns tested in low-speed rig. (*a*) $A_D = 0$, (*b*) $A_D = 0.34$, (*c*) $A_D = 0.17$, $n_D = 1$, (*d*) $A_D = 0.17$, $n_D = 2$, (*e*) $A_D = 0.17$, $n_D = 3$, and (*f*) $A_D = 0.22$, $n_D = 2$.

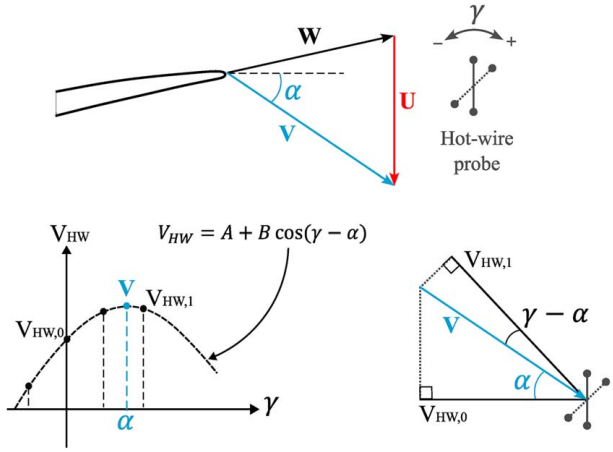

Fig. 6 Hot-wire angle calculation

Using a once-per-revolution trigger signal on the rotor shaft in combination with the hot-wire probe measurements, it was possible to obtain an ensemble average of the flow field. The ensemble-averaged hot-wire velocity at each traverse point was obtained using Eq. (4), where J is the number of rotor revolutions for averaging. In all results shown in this article, $J = 50$ was used to provide a detailed blade-to-blade flow field

$$V_{\text{ens}} = \frac{1}{J}\sum_{j=1}^{J} V_j \tag{4}$$

Measurement uncertainties for both the five-hole probe and hot-wire measurements were calculated as described in Appendix. Table 3 shows a summary of the uncertainties for the main quantities of interest: swirl angle U_α, total pressure U_{P_0}, and flow velocity U_V.

Computational Methods

Both the undamaged fan and axisymmetric tip damage fan cases were modeled using steady Reynolds-averaged Navier–Stokes (RANS) using the GPU code `Turbostream` [14]. Fully turbulent boundary layers were assumed everywhere, and the Spalart–Allmaras turbulence model with adaptive wall functions was used. The mesh was set up with a y^+ below 5 on all solid walls.

The computational domain includes both rotor and stator, as well as an inlet duct to provide the right boundary conditions at the fan face and a choked exit nozzle to control the mass flowrate and thus the windmill operating point. Single-passage simulations were used, as the $A_D = 0$ and $A_D = 0.34$ cases modeled are both axisymmetric. As shown in Fig. 7, at the inlet, the total pressure P_0 and temperature T_0 were set, as well as axial inlet flow ($\alpha, \zeta = 0°$). A mixing plane was placed between rotor and stator, and a constant static pressure P condition was used at the nozzle exit.

A multiblock mesh was generated in NUMECA IGG/AUTOGRID5, with H-mesh at inlet and exit ducts, and O4H mesh in rotor and stator blocks, which uses an O-mesh around the blades surrounded by 4 H-mesh blocks to join the O-mesh to the adjacent blocks. The full single-passage mesh comprises 3.4×10^6 cells for the

Table 3 Maximum measurement uncertainty normalized by local value

	U_α/α (%)	$U_{P_0}/(P_0 - P)$ (%)	U_V/V (%)
Five-hole probe	3.03	2.52%	1.78
Hot-wire probe	1.92	–	2.45

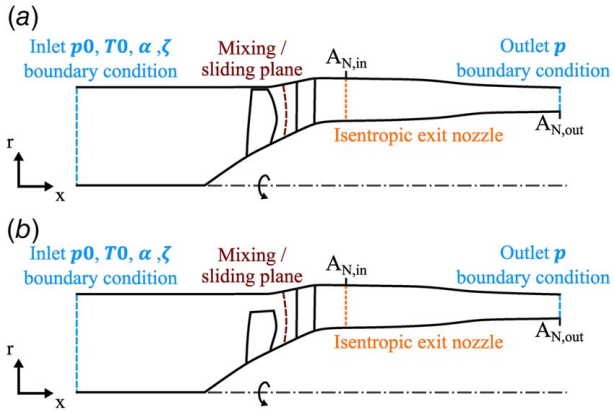

Fig. 7 Computational domain for RANS simulations. (*a*) Undamaged fan. (*b*) Axisymmetric tip-damaged fan.

undamaged fan case ($A_D = 0$) and 3.8×10^6 cells for the axisymmetric tip damage case ($A_D = 0.34$).

To achieve the windmill condition, the fan rotational speed Ω and mass flowrate $\dot{m}$ were iterated until the overall specific power output from the fan $P_{\text{out}}/\dot{m}$ is zero, Eq. (5)

$$\frac{P_{\text{out}}}{\dot{m}} = \Delta h_0 = \frac{2\pi\rho}{\dot{m}} \int_{r_{\text{hub}}}^{r_{\text{cas}}} r^2 V_x \Omega \left(r\Omega - V_x \tan\beta_4\right) \mathrm{d}r = 0 \tag{5}$$

Figure 8 compares the pitchwise mass average of the key windmill nondimensional values from CFD and experimental measurements. Good agreement can be seen in the axial velocity distribution at both rotor inlet ($V_{x3}/\overline{U}$) and rotor exit ($V_{x4}/\overline{V_{x1}}$) as well as in the rotor work distribution ($rV_{\theta 4}/\overline{rU}$). This agreement supports the use of a low-speed rig to investigate windmill.

Axisymmetric Tip Damage

Figure 9 plots the windmill operating points for both the axisymmetric tip damage ($A_D = 0.34$) and undamaged ($A_D = 0$) fan. Lines corresponding to Eq. (6) are also shown, where a flow coefficient $\phi = 2.29$ was used for the undamaged fan and $\phi = 5.87$ for the axisymmetric tip-damaged fan. These show that for a given nondimensional mass flowrate, the fan with axisymmetric tip damage windmills at a rotational speed 61% lower than the undamaged case.

$$\tilde{U} = \frac{\overline{U}}{\sqrt{c_p T_{01}}} = \frac{\overline{V}_{x3}}{\overline{V}_{x1}} \frac{1}{\phi} \frac{\rho_{01}}{\rho_1} \frac{\gamma - 1}{\gamma} \tilde{m} \tag{6}$$

The flow coefficient at windmill ϕ can be calculated from the mass-averaged rotor inlet axial velocity $\overline{V}_{x3}$ and the rotor exit conditions at the zero-work radius (Eq. (7)).

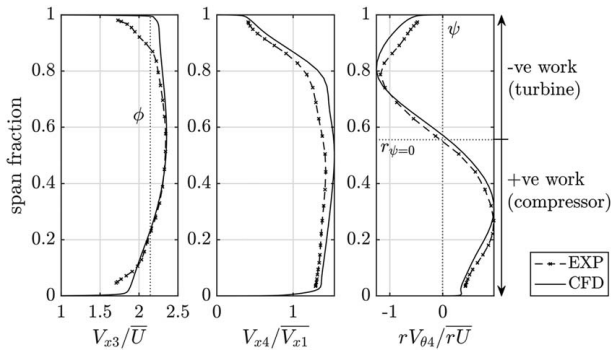

Fig. 8 Five-hole probe measurements comparison to low-speed rig CFD

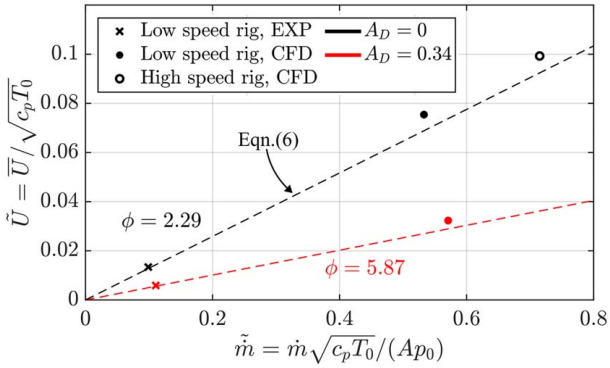

Fig. 9 Windmill characteristic for undamaged and axisymmetric tip damage cases

$$U_{\psi=0} = V_{x4} \tan\beta_4 \rightarrow \overline{U} = U_{\psi=0} \times \frac{\overline{r}}{r_{\psi=0}}$$
$$\phi = \frac{\overline{V}_{x3}}{\overline{U}} = \frac{\overline{V}_{x3}}{V_{x4} \tan\beta_4} \times \frac{r_{\psi=0}}{\overline{r}} \tag{7}$$

Figure 10 shows a radial redistribution of flow toward the casing where the blade tip has been removed, with a dip in velocity just below the tip damage region. The undamaged fan shows a large drop in axial velocity toward the casing, as shown in Refs. [2,8] to correspond with the presence of a vortex on the rotor pressure side.

When the fan is undamaged, the zero-work radius is at 56% span. In the case of the $A_D = 0.34$ axisymmetric tip-damaged fan, there is no work output from the fan above 75% span where the blade tips have been removed. The zero-work point has shifted down the span, from 56% to 41%. The shift in the zero-work point leads to a reduction in blade speed, due to the lower blade exit metal angle at inboard sections of the span. This is illustrated in Fig. 11, where the blade section for the zero-work radius in the case of axisymmetric tip damage has a much lower exit metal angle and thus lower blade speed U.

The phase-averaged hot-wire results shown in Fig. 12 detail the rotor exit flow field. In the case where the fan is undamaged, a region of low axial velocity can be seen at the casing. When there is damage to the blade tips, this region of low axial velocity moves to the damaged blade tip, and flow accelerates above the tip of the rotor.

$$\omega_x/\Omega = [\nabla \times (v, w)]/\Omega \tag{8}$$

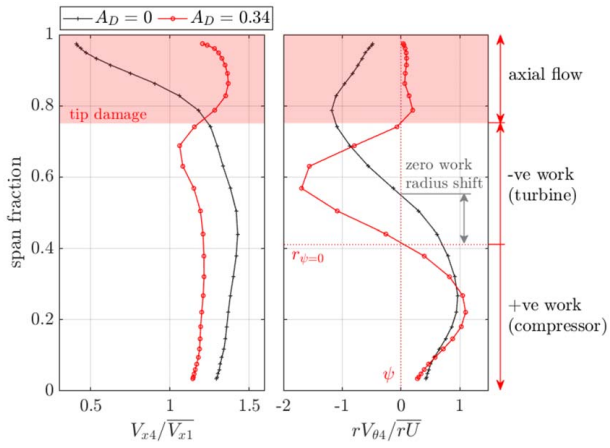

Fig. 10 Pitchwise averaged five-hole probe measurements at rotor exit (station 4)

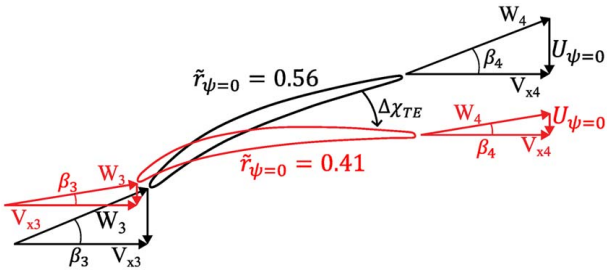

Fig. 11 Velocity triangles at zero-work radius for axisymmetric tip damaged and undamaged fans

Figure 13 shows the regions of low axial velocity seen at the undamaged fan casing and damaged fan blade tip correspond to regions of high streamwise vorticity, ω_x/Ω, calculated as per Eq. (8). This indicates the presence of the pressure side vortex shown in Fig. 1. The contours in Fig. 13 show the tip vortex for the damaged case, $|\omega_x/\Omega| > 500$, are stronger than the undamaged case

$$\zeta = \frac{T_{\text{out}}(s_{\text{out}} - s_{\text{in}})}{0.5V_{\text{in}}^2} \tag{9}$$

It is also of interest to predict how much loss will be generated through the fan stage with and without damage, as this is directly related to the drag at windmill. Figure 14 shows where entropy gets generated through the rotor in the form of the entropy loss coefficient from Eq. (9), where V_{in} is the inlet velocity in the relative frame for a rotor row and in the absolute frame for a stator row. These results show that the main source of entropy in the rotor stage is the pressure side vortex for both the undamaged fan (Fig. 14(*a*)) and the fan with axisymmetric tip damage (Fig. 14(*b*)). The undamaged fan casing vortex leads to entropy loss coefficient values as high as $\zeta = 1.8$, due to the vortex

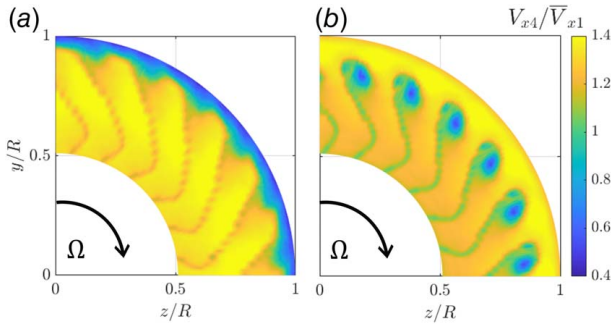

Fig. 12 Hot-wire measurements of rotor exit axial velocity for axisymmetric cases: (*a*) $A_D = 0$ and (*b*) $A_D = 0.34$

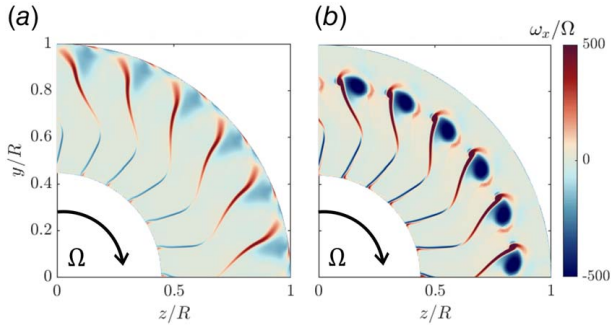

Fig. 13 CFD streamwise vorticity contours at rotor exit. (*a*) $A_D = 0$ and (*b*) $A_D = 0.34$.

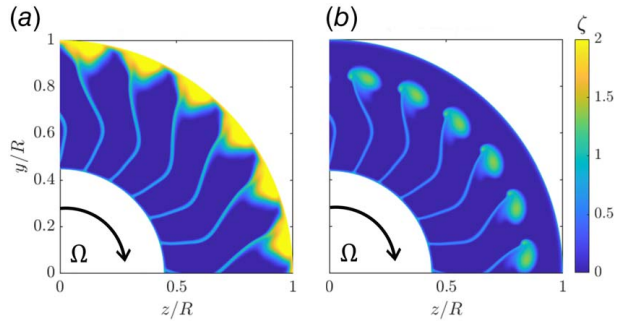

Fig. 14 CFD entropy loss coefficient contours at rotor exit: (*a*) $A_D = 0$ and (*b*) $A_D = 0.34$

mixing with slow-moving flow in the casing boundary layer. By comparison, the loss coefficient due to the vortex at the damaged blade tip is around $\zeta = 1.2$.

Mass-averaged entropy loss coefficients are shown in Fig. 15. The loss generated through the rotor is lower in the case of axisymmetric damage to the blade tip ($\zeta = 0.2$ compared to $\zeta = 0.3$ for an undamaged fan). This matches what is shown in Fig. 14, as there is more entropy generated in the vortex region at the casing due to the large reduction in flow velocity. Most of the stage loss is generated in the stator row, where the entropy loss coefficients are as high as $\zeta = 0.5$ for both the damaged and undamaged fan cases.

Previous studies have shown that when the fan is windmilling, the low rotational speed will cause highly off-design angles at rotor exit, and thus, high negative incidence onto the stator [1,15]. These negative incidence angles lead to the flow separating on the stator pressure side without reattachment toward the trailing edge. The large flow separation leads to the high losses through the stator in Fig. 15.

Figure 16 shows that incidence onto the stator is more negative for the damaged case than the undamaged case over lower span sections due to the reduction in fan rotational speed. Above 75% span where the blade tips are removed, the flow approaches the stator with zero swirl, which leads to a lower incidence than the undamaged case. In both cases shown in Fig. 16, the region of the largest flow separation corresponds to the highest negative incidence point in the angle distribution ($i_{\max}$).

Dufour et al. [3] showed that the region of highest loss in the stator corresponds to the formation of a counter-rotating vortex within the flow separation, which leads to high mixing. This region of high loss can be seen in both the undamaged and

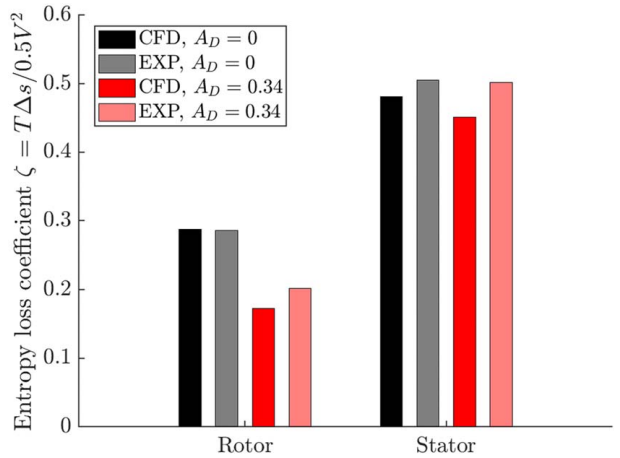

Fig. 15 Undamaged ($A_D = 0$) and axisymmetric tip damage fan ($A_D = 0.34$) blade row losses

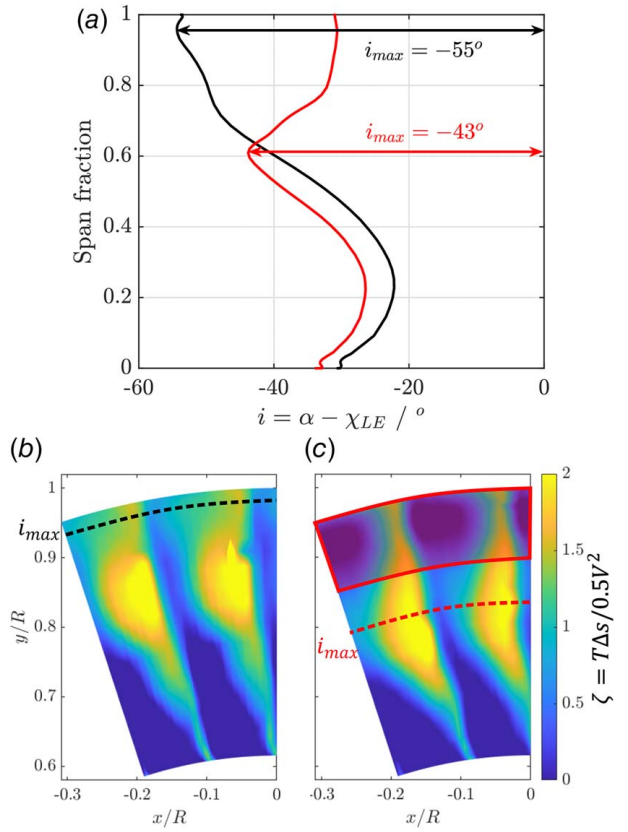

Fig. 16 Stator incidence and loss contours obtained from five-hole probe measurements: (*a*) Stator spanwise incidence distribution, (*b*) $A_D = 0$, and (c) $A_D = 0.34$

damaged cases and simply shifts down the span in the $A_D = 0.34$ case due to the change in incidence distribution. This explains the similar levels of stator loss shown in Fig. 16.

Non-Axisymmetric Damage

Blade-to-blade differences in the flow field for the non-axisymmetric tip damage cases are shown in Fig. 17 using phase-averaged hot-wire measurements of rotor exit velocity. In all cases, there is a large drop in axial velocity near the casing when the blade is undamaged. This is caused by the rotor pressure side vortex, shown in Fig. 1. The casing vortex is largest and leads to a lower V_x when the preceding blade is damaged and the vortex can expand into the space above the damaged blade. By comparison, when there are several undamaged blades in a row as in Figs. 17(*b*) and 17(*c*), the casing vortex appears similar to that in the undamaged fan (see Fig. 12(*a*)).

For damaged blades in Fig. 17, there is a drop in axial velocity around 75% span, as was shown for the axisymmetric damage case. This indicates the presence of the tip vortex, which is contained by the high-speed flow above the damaged blades.

Figure 18 compares spanwise distributions for three non-axisymmetric tip damage cases with the undamaged and damaged axisymmetric cases. The radial variations of $V_{x4}/\overline{V}_{x1}$ for the nonaxisymmetric cases are similar to the average of the two axisymmetric cases. This average has the same equivalent damage, $A_D = 0.17$, as the non-axisymmetric cases are shown. This indicates that the impact of non-axisymmetric damage on the axial velocity field and flow blockage could be estimated by linearly combining axisymmetric cases.

The work distribution in Fig. 18, however, shows that averaging the work distributions of the axisymmetric undamaged and damaged cases does not match the non-axisymmetric tip damage cases. The non-axisymmetric tip damage cases have a zero-work point around 52% span, compared to 45% span for the average of the undamaged and axisymmetric damage cases. As can be seen in the $V_{x3}/\overline{U}$ plot in Fig. 18, the higher zero-work radius corresponds to a flow coefficient in the non-axisymmetric tip damage cases that is close to that of the undamaged fan. This is a result

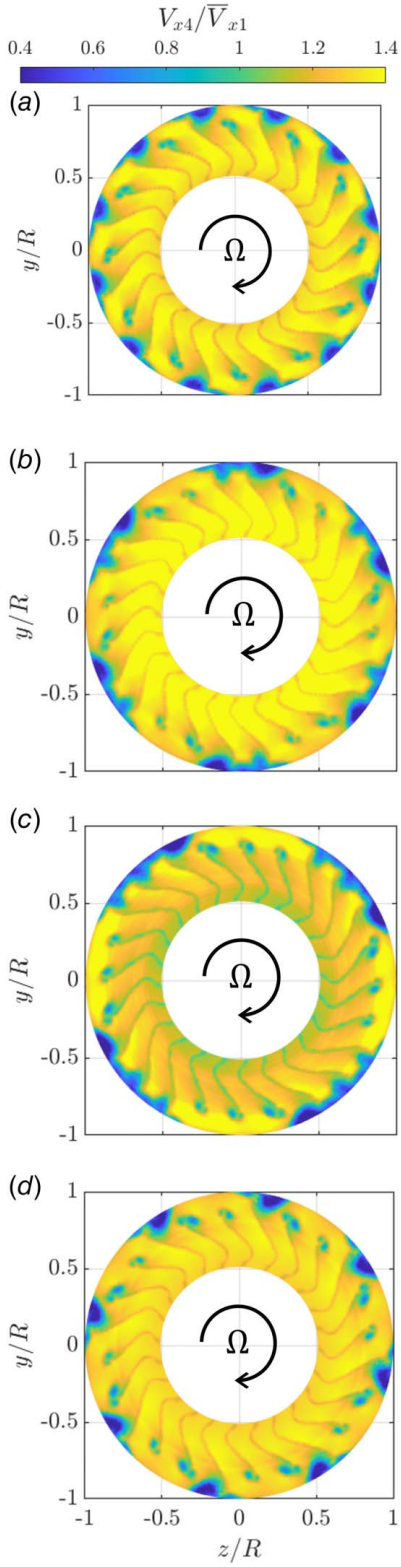

Fig. 17 Rotor exit hot-wire measurements. (*a*) $A_D = 0.17$, $n_D = 1$, (*b*) $A_D = 0.17$, $n_D = 2$, (c) $A_D = 0.17$, $n_D = 3$, (d) $A_D = 0.22$, $n_D = 2$.

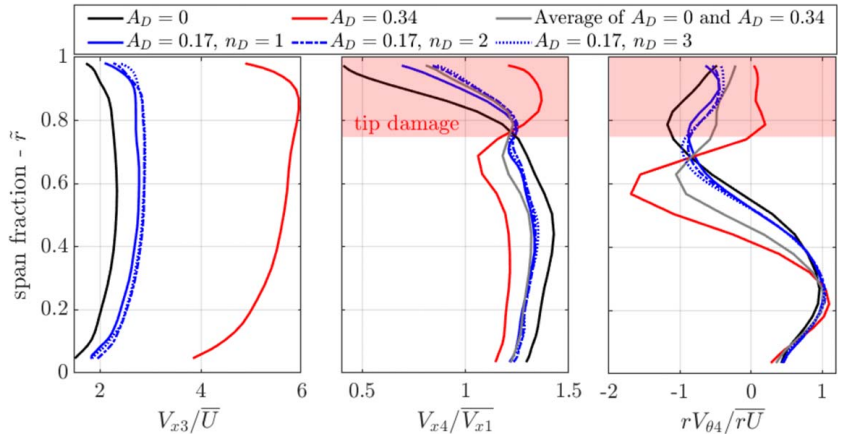

Fig. 18 Comparison of pitchwise averaged five-hole probe measurements for varying damage

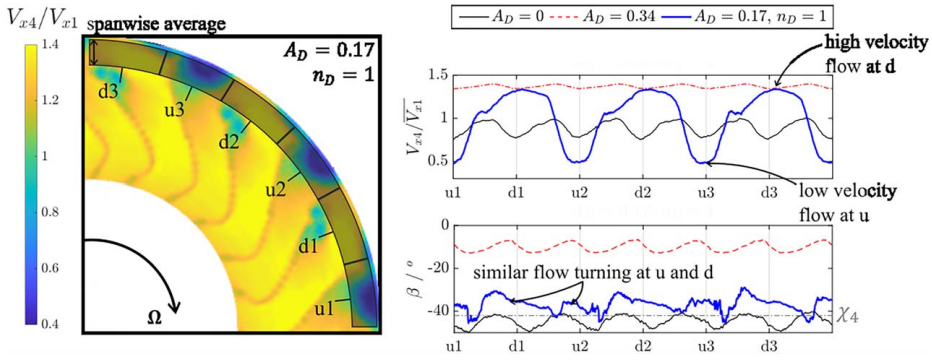

Fig. 19 Axial velocity and relative flow angle mass averaged between 75% and 95% span

of work being generated above the tips of damaged blades in the non-axisymmetric cases.

Figure 19 shows the rotor exit axial velocity $V_{x4}/\overline{V}_{x1}$ and relative flow angle β_4 extracted directly from hot-wire data for the tip damage region for 6-fan blade passages or 1/4 annulus. The data have been mass averaged in the spanwise direction between 75% and 95% to produce plots of the circumferential variations between the individual fan blades.

The results from the $A_D = 0.17$, $n_D = 1$ case are compared to the undamaged fan and the axisymmetric damage case. With non-axisymmetric damage, two distinct regions have been identified based on the values of $V_{x4}/\overline{V}_{x1}$. Points downstream of an undamaged blade TE, marked u1/u2/u3, show a drop in axial velocity ($V_{x4}/\overline{V}_{x1} = 0.5$), which is caused by the vortex near the casing. Above the damaged blade tips, there is flow redistribution and the axial velocity increases to the value in the axisymmetric damage case ($V_{x4}/\overline{V}_{x1} = 1.4$). Points downstream of a damaged blade tip have been marked d1/d2/d3 in Figs. 19 and 21.

The rotor exit relative flow angle in Fig. 19 remains close to −40 deg both in the undamaged (u1/u2/u3) and damaged (d1/d2/d3) regions. This shows that the flow is still turned above the damaged blade tips and the exit relative flow angle follows the exit metal angle of the undamaged fan across all the blade passages.

Figure 20 shows two velocity triangles for flow at 85% span for non-axisymmetric damage: one is for flow above a damaged blade and the other is for the tip region of an undamaged blade. The variation in axial velocity with a similar exit relative swirl angle leads to the sign of the exit absolute tangential velocity V_{θ_4} switching from negative to positive between the two regions. This implies a switch from negative turbine-style work downstream of the damaged tips to positive compressor-style work downstream of the undamaged blades.

Figure 21 shows the local work coefficient based on the Euler work equation given in Eq. (10). The fully undamaged fan tip work remains negative over the full annulus, and the axisymmetric tip damage fan produces zero work overall at the tip, with Δh_0 oscillating around zero. The nonaxisymmetric damage cases show a work output at the tip which varies between compressor and turbine work as demonstrated by the velocity triangles in Fig. 20. Work in the tip region for the nonaxisymmetric tip damage cases will thus depend on the local V_{x4} and $\tan\beta_4$ in Eq. (10)

$$\frac{\Delta h_0}{\overline{U}^2} = \frac{U_4^2}{\overline{U}^2} + \frac{U_4}{\overline{U}}\frac{\overline{V}_{x3}}{\overline{U}}\frac{V_{x4}}{\overline{V}_{x3}}\tan\beta_4 \tag{10}$$

This is further supported by Fig. 22, which shows the rotor exit relative swirl averaged at u1/u2/u3 and d1/d2/d3 for each non-axisymmetric tip damage case. This provides representative values in the undamaged and damaged regions respectively, which can help explain the variation in work around the annulus

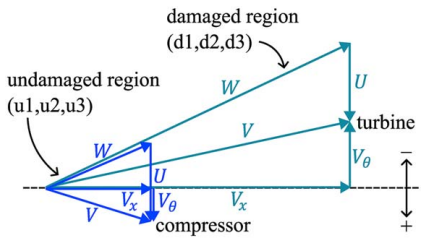

Fig. 20 Velocity triangles at 85% span for nonaxisymmetric damage case, $A_D = 0.17$, $n_D = 1$

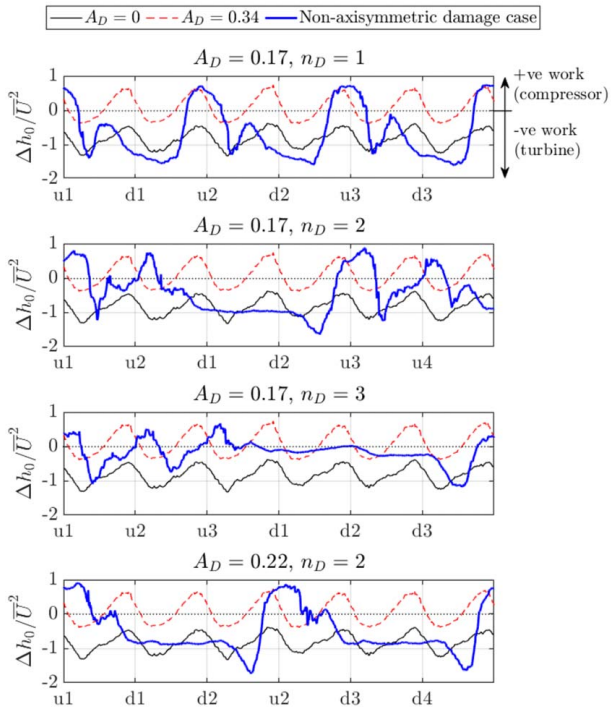

Fig. 21 Circumferential variation of rotor work output averaged over 75–95% span

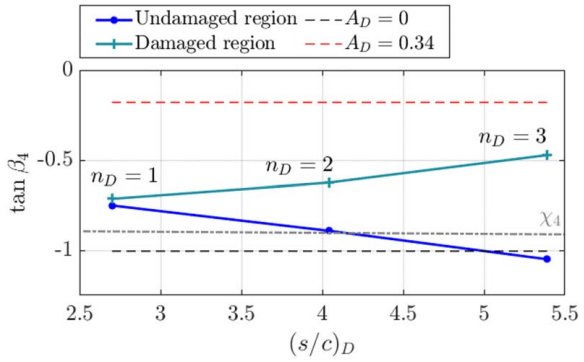

Fig. 22 Rotor exit relative swirl angle as a function of damage pitch to chord, averaged from 75% to 95% span in damaged and undamaged region

shown in Fig. 21. The exit swirl angle β_4 in the undamaged region increases with increasing $(s/c)_D$ as there is more flow turning with a greater number of consecutive undamaged blades. In the damaged region, the exit swirl angle decreases as the number of consecutive damaged blades increases.

Figure 17 shows that the axial flow velocity is consistently high above damaged blades, d1/d2/d3. In this region, the amount of turbine work depends mainly on the exit relative flow angle β_4. As n_D and the damage pitch-to-chord $(s/c)_D$ increase, the blades on either side of the damaged region provide less turning, as is shown in Fig. 22. This decrease in turning leads to reduced work in the damaged region with increasing n_D as shown in Fig. 21.

Above undamaged blades, u1/u2/u3, Fig. 17 shows that the axial velocity is low but varies across the passages. The leading undamaged blade has a region of high blockage that reduces the axial velocity and moves the blade tip region toward compressor operation as in the velocity triangle shown in Fig. 20. When there are several undamaged blades in a row, as in Figs. 17(*b*) and 17(*c*),

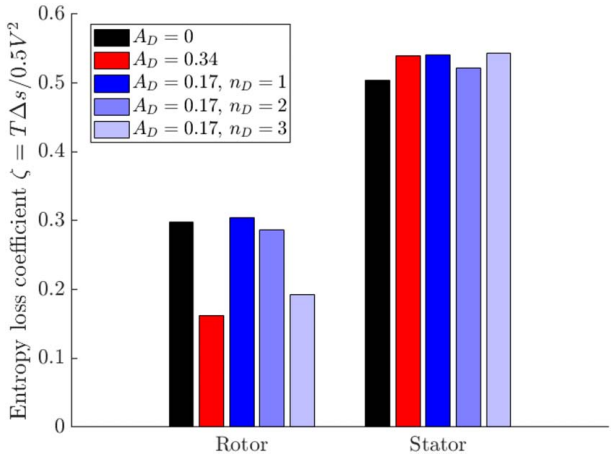

Fig. 23 Blade row losses computed from five-hole probe data for different fan damage cases in windmill condition

the axial velocity increases in the following blades, moving the blade tip toward turbine operation. This can be thought of as extending the *Vx* and thus *W* vectors in the undamaged region velocity triangle from Fig. 20 while keeping *U* constant. Overall, in the undamaged tip region, the work is more influenced by the axial velocity variations than the relative angle changes. This is reflected in Fig. 21, as Δh_0 decreases in the undamaged region for the cases $A_D = 0.17$, $n_D = 2, 3$.

It is this additional work being produced in the damaged tip region that is not accounted for in current models of the windmill condition. This significantly alters the work distribution compared to an axisymmetric tip damage case, as shown in Fig. 18. When damage is axisymmetric, there is no work being produced at the tip, and the whole work distribution must shift downward to maintain the windmill condition. When the damage is non-axisymmetric, there is work being generated at the tip, which leads to the work distribution being similar to that of an undamaged fan over the majority of the span, and thus, a very small shift in the windmill zero-work radius and rotational speed.

Figure 23 shows that the majority of the loss comes from the stator and is similar for all the cases tested. The rotor loss decreases with increasing $(s/c)_D$. This might be caused by the increasing number of consecutive damaged and undamaged blades, which both reduce the difference in axial velocity between the damaged and undamaged tip passages and decrease the number of free shear layers, thus leading to lower mixing loss.

Conclusions and Future Work

The flow field of a fan in windmill condition has been investigated, for both an undamaged fan and fans with axisymmetric and non-axisymmetric tip damage.

For a fan with 25% span axisymmetric tip damage, it was found:

(1) There is no work produced in the tip region such that the work distribution shifts toward the hub, with the zero-work radius location moving from 56% span to 40% span.
(2) This shift in zero-work radius leads to a reduction in exit flow angle and thus a large increase in flow coefficient from $\phi = 2.19$ to $\phi = 5.59$ and reduction in blade speed of 61%.
(3) The pressure side vortex emerges from the damaged blade tip rather than the casing.
(4) The reduction in the size of the pressure side vortex leads to a nearly 50% reduction in rotor loss for axisymmetric tip damage; however, due to the incidence of the stator being highly negative with such low blade speed, the loss produced in the stator is similar to that of the undamaged fan.

For non-axisymmetric tip damage:

(1) The flow velocity downstream of the rotor is shown to be a combination of the undamaged fan flow field, with a large blockage at the casing in the undamaged blades, and the axisymmetric tip damage case, with a high axial velocity above the damaged tips and low axial velocity at the tip where the vortex gets convected.
(2) The work distribution is largely dependent on the rotor exit flow angles, which vary significantly with damage pitch to chord. In particular, the turning of higher velocity flow in the damaged tip region has the largest influence on the tip work output.
(3) For fewer consecutive damaged blades, the fan is able to introduce a nearly 40-deg relative swirl in the fast-moving flow over the damaged tip region. However, for more consecutive damaged blades, there will be low turning of lower velocity flow in the damaged tip region, leading to less turbine work.
(4) The rotor loss reduces with damage pitch-to-chord. The stator loss is independent of fan damage and comparable to that of the axisymmetric cases.

These findings will inform improved models to predict the drag and rotational speed of low pressure ratio fan designs with a variety of fan damage patterns. These models will be developed and demonstrated in future work.

Acknowledgment

The authors want to thank Rolls-Royce plc. and EPSRC for providing the funding to conduct this research. Thanks also go to Stephane Baralon for lending his industry expertise and providing advice. Ewan Gunn is acknowledged for his help in setting up the rig CFD. Thanks to Luke Arnold and Liam Cohen for their contribution in manufacturing and assembling the rig redesign.

Conflict of Interest

There are no conflicts of interest.

Data Availability Statement

The authors attest that all data for this study are included in the article.

Nomenclature

c = Blade chord
i = Rotor incidence (deg)
j = Cycle counter for hot-wire ensemble average
r = Polar radial coordinate
s = Blade pitch
x = Cartesian x-coordinate, aligned with axial direction
y = Cartesian y-coordinate
z = Cartesian z-coordinate
E = Hot-wire voltage
J = Number of cycles to average over in ensemble average
N = Total number of fan blades
U = Rotor blade speed (m/s), or measurement uncertainty.
V = Flow velocity in absolute frame of reference (m/s)
W = Flow velocity in relative frame of reference (m/s)
$\dot{m}$ = Mass flowrate (kg/s)
h_0 = Specific stagnation enthalpy
n_D = Number of consecutive damaged fan blades
r_D = Tip radius of damaged blade
A_D = Fraction of damage to the fan face area
N_D = Total number of damaged fan blades
P_{out} = Fan power output

Greek Symbols

α = Flow swirl angle in absolute frame of reference (deg)
β = Flow swirl angle in relative frame of reference (deg)
γ = Hot-wire probe rotation angle (deg) (or specific heat ratio $\gamma = c_p/c_v$)
ζ = Radial flow angle at inlet in CFD simulations (deg)
θ = Polar tangential coordinate
ρ = Density (kg/m^3)
χ = Blade metal angle (deg)
ω = Vorticity (1/s)
Ω = Rotor angular velocity (rad/s)

Superscripts and Subscripts

0 = Stagnation value
1 = Value at rig inlet
3 = Value at rotor inlet
4 = Value at rotor exit
5 = Value at stator exit
cas = Quantity at rotor casing
ens = Ensemble-averaged quantity
hub = Quantity at rotor hub
tip = Quantity at blade tip
$\psi = 0$ = Quantity at windmill zero-work radius

Dimensionless Groups

Re = Reynolds number, $\rho V c/\mu$
M = Mach number, $V/\sqrt{\gamma RT}$
$\tilde{m}$ = Nondimensional mass flow, $\dot{m}\sqrt{c_p T_0}/A p_0$
$\tilde{U}$ = Nondimensional blade speed, $\overline{U}/\sqrt{c_p T_0}$
ϕ = Flow coefficient, $V_x/\overline{U}$
ψ = Stage loading coefficient, $\Delta h_0/\overline{U}^2 = \Delta(UV_\theta)/\overline{U}^2$
ζ = Loss coefficient $T\Delta s/0.5V^2$

Acronyms

CFD = Computational fluid dynamics
LE = Leading edge
RANS = Reynolds-averaged Navier–Stokes
TE = Trailing edge

Appendix: Measurement Uncertainties

Measurement uncertainties in both the five-hole probe and hot-wire measurements were calculated using the method proposed by Abernethy et al. [16], where the bias and precision errors for the measured quantities (pressures in the case of the five-hole probe, and voltage in the case of the hot wire) can be propagated to obtain the uncertainty in the derived quantities using influence coefficients.

1 Five-Hole Probe Uncertainties. The five-hole probe calibration coefficients were used to obtain the angles, flow velocities and pressures in the rig by interpolating in a calibration map. The probe pressures are numbered P_1 to P_5, where 1 is the central hole pressure, and the calibration jet total and static pressures P_0 and P_s are also known. The coefficients were found as follows:

$$C_\alpha = \frac{P_4 - P_5}{P_{\text{ref}}} \quad C_\xi = \frac{P_2 - P_3}{P_{\text{ref}}} \quad C_{P_0} = \frac{P_0 - P_1}{P_{\text{ref}}} \quad C_{P_s} = \frac{P_0 - P_s}{P_{\text{ref}}}$$

The bias error in the pressure scanner is $B_P = 4.137$ Pa, and the precision errors for each probe hole are $S_1 = 2.08$ Pa, $S_2 = 2.23$ Pa, $S_3 = 3.39$ Pa, $S_4 = 3.21$ Pa, and $S_5 = 3.38$ Pa. For each coefficient C_x, the uncertainty U_{C_x} is found as follows:

$$U_{C_x} = \sqrt{B_{C_x}^2 + S_{C_x}^2}\, B_{C_x}^2 = \sum_{i=1}^{5}\left(\frac{\partial C_x}{\partial P_i}\right)^2 \cdot B_P^2 \quad S_{C_x}^2 = \sum_{i=1}^{5}\left(\frac{\partial C_x}{\partial P_i}\right)^2 \cdot S_{P_i}^2$$

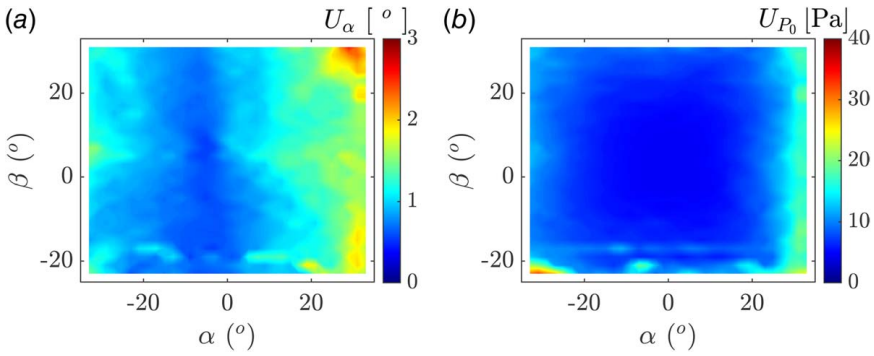

Fig. 24 Uncertainty in measured five-hole probe values. (*a*) Swirl angle and (*b*) total pressure.

where the terms $\partial C_x/\partial P_i$ are the influence coefficients from each pressure uncertainty on the coefficients. This process can then be extended to find the angle uncertainties using the influence coefficients with respect to the calibration coefficients ($\partial\alpha/\partial C_\alpha$, etc.) and total and static pressure measurement uncertainties, which can in turn be used to find the velocity uncertainty, as this is a derived quantity from the pressures and angles:

$$V = \sqrt{\frac{2(P_0 - P_s)}{\rho}} \quad V_\theta = V \sin\alpha \quad V_x = V \cos\alpha \cos\xi$$

The resulting uncertainties for each quantity measured with the five-hole probe are thus dependent on the flow angle. Figure 24(*a*) shows that the angle uncertainty reaches a maximum of 3 deg at the edges of the calibration map (which corresponds to swirl angle of $35\,\text{deg} \le \alpha \le 40\,\text{deg}$), Fig. 24(*b*) shows that the total pressure reaches a maximum uncertainty of around 30 Pa.

These uncertainties in pressure and angle translate to velocity uncertainties which stay generally below 0.5% of the local velocity, with a maximum of around 3% of local velocity.

2 Hot-Wire Uncertainties. Uncertainties in the velocity measurements can be obtained by propagating the errors in voltage in a similar way to what was done for the five-hole probe error analysis. The influence coefficient $\partial V/\partial E$ can be calculated from King's law. The bias error in voltage is canceled out, as there will be the same error in E and E_0, therefore only the voltage precision error S_E is required, the uncertainty in velocity due to uncertainties in voltage measurement can then be calculated as

$$U_V = \frac{\partial V}{\partial E} S_E$$

This was found to be $(U_V/V)_{\max} = \pm 0.53\%$ of local velocity. Further uncertainty is introduced by the curve fit to obtain the King's law equation. By comparing the calibration values to those of the fitted equation, the maximum error from the curve fit was found to be $(\Delta V/V)_{\max} = \pm 2.4\%$. This leads to an overall maximum error in velocity from the King's law calibration of $|\Delta V/V|_{\max} = \pm 2.453\%$.

Errors in the flow angle calculation depend on both the error in velocity U_V and the bias error in hot-wire rotation due to uncertainties from the motor, $B_\gamma = \pm 0.5$ deg. The bias error dominates the overall uncertainty, as it is over an order of magnitude greater than the uncertainty due to the velocity calibration. The maximum uncertainty in angle is expected to be $U_\alpha = \pm 0.77$ deg.

References

[1] Prasad, D., and Lord, W. K., 2010, "Internal Losses and Flow Behavior of a Turbofan Stage at Windmill," ASME J. Turbomach., **132**(3), p. 031007.
[2] Gunn, E. J., and Hall, C. A., 2016, "Loss and Deviation in Windmilling Fans," ASME J. Turbomach., **138**(10), p. 101002.
[3] Dufour, G., García Rosa, N., and Duplaa, S., 2015, "Validation and Flow Structure Analysis in a Turbofan Stage at Windmill," Proc. Inst. Mech. Eng., Part A: J. Power Energy, **229**(6), pp. 571–583.
[4] García Rosa, N., Dufour, G., Barènes, R., and Lavergne, G., 2015, "Experimental Analysis of the Global Performance and the Flow Through a High-Bypass Turbofan in Windmilling Conditions," ASME J. Turbomach., **137**(5), p. 051001.
[5] Binder, N., Courty-Audren, S. K., Duplaa, S., Dufour, G., and Carbonneau, X., 2015, "Theoretical Analysis of the Aerodynamics of Low-Speed Fans in Free and Load-Controlled Windmilling Operation," ASME J. Turbomach., **137**(10), p. 101001.
[6] García Rosa, N., Thacker, A., and Dufour, G., 2021, "Periodic Flow Structures in a Turbofan Fan Stage in Windmilling," Proc. Inst. Mech. Eng., Part G: J. Aerospace Eng., **235**(4), pp. 501–512.
[7] Zhang, J., Chen, Y., Jin, L., and Tang, X., 2022, "Free-Windmilling Speed Prediction Based on Aerodynamic Similarity of an Axial Wide-Chord Fan," J. Propul. Power, **39**(1), pp. 1–13.
[8] Mohankumar, B., and Wilson, M. J., 2017, "Rotational Speed of a Damaged Fan Operating at Windmill," Proceedings of the 12th European Conference on Turbomachinery, Fluid Dynamics and Thermodynamics, Stockholm, Sweden, Apr. 3–7.
[9] Zhang, J., Chen, Y., Jin, L., Tang, X., and Wang, Z., 2023, "Evaluation of the Free-Windmilling Rotational Speed of a Damaged Wide-Chord Fan Rotor," Aerospace Sci. Technol., **140**, p. 108421.
[10] Gunn, E. J., Tooze, S. E., Hall, C. A., and Colin, Y., 2013, "An Experimental Study of Loss Sources in a Fan Operating With Continuous Inlet Stagnation Pressure Distortion," ASME J. Turbomach., **135**(3), p. 051002.
[11] Castillo Pardo, A., and Hall, C. A., 2021, "Aerodynamics of Boundary Layer Ingesting Fuselage Fans," ASME J. Turbomach., **143**(4), p. 041007.
[12] Denton, J. D., 1978, "Throughflow Calculations for Transonic Axial Flow Turbines," ASME J. Eng. Power, **100**(2), pp. 212–218.
[13] Bruun, H., 1995, *Hot-Wire Anemometry: Principles and Signal Analysis*, Oxford Science Publications, Oxford University Press, New York.
[14] Brandvik, T., and Pullan, G., 2011, "An Accelerated 3D Navier–Stokes Solver for Flows in Turbomachines," ASME J. Turbomach., **133**(2), p. 021025.
[15] Thacker, A., García Rosa, N., and Dufour, G., 2017, "Experimental Analysis of the Unsteady, Turbulent Flow Through the Fan Stage of a High-Bypass Turbofan in Windmilling Conditions," Proceedings of the 12th European Conference on Turbomachinery, Fluid Dynamics and Thermodynamics, Stockholm, Sweden, Apr. 3–7.
[16] Abernethy, R. B., Benedict, R. P., and Dowdell, R. B., 1985, "ASME Measurement Uncertainty," ASME J. Fluids Eng., **107**(2), pp. 161–164.